Asian Journal of Chemistry; Vol. 38, No. 9 (2026), 2268-2280
ASIAN JOURNAL OF CHEMISTRY
https://doi.org/10.14233/ajchem.2026.36271

Charge Transport and Magnetoresistive Mechanisms in Samarium-Doped Manganite Nanoparticles and Their Polypyrrole Nanocomposite

SUPRIYA DUTTA[1], SOUMEN RAKSHIT[2], PARESH CHANDRA JANA[2], ANIMESH SAHANA[1,*] and KAJAL GUPTA[1,*]

[1]Department of Chemistry, Nistarini College, Deshbandhu Road, Purulia-723101, India
[2]Department of Physics, Vidyasagar University, Paschim Medinipur-721102, India

*Corresponding authors: E-mail: sahana.animesh@gmail.com; kajaldgpnit@gmail.com

Received: 20 April 2026 *Accepted*: 29 June 2026 *Published online*: 5 September 2026 AJC-22455

A detailed investigation of charge transport, encompassing direct-current (DC) and alternating-current (AC) conduction, was performed for samarium-doped manganite nanoparticles and their polypyrrole (PPy)-based nanocomposites. The electrical transport characteristics of the pristine manganite and nanocomposite systems were examined as a function of temperature, magnetic field and samarium concentration. The pristine manganite exhibits characteristic polycrystalline magnetoresistance (MR), with MR increasing from ~55% for the lowest samarium concentration (M1) to ~75% for the highest concentration (M5) at 50 K. Spin-polarized tunneling across grain boundaries constitutes the dominant MR mechanism, with the temperature dependence supporting the role of suppressed spin fluctuations. The nanocomposites exhibit anomalous, fluctuation-like field-dependent MR behaviour that varies with temperature and samarium concentration, with the effect being most pronounced at lower samarium concentrations over the 50-250 K temperature range. This behaviour is attributed to the competition between weak localization and charge-carrier delocalization within a core-shell architecture, mediated by intermediate exchange coupling and the incorporation of polypyrrole. The distinct transport and magnetoresistance responses of the manganite nanoparticles and PPy-based nanocomposites provide insight into the interplay between grain-boundary effects, magnetic exchange interactions and polymer-mediated charge transport.

Keywords: Magnetoresistance, Manganite, Nanocomposite, Spin-polarized tunneling, Spin fluctuation.

INTRODUCTION

Perovskite-type oxides containing transition metals exhibit a diverse range of electrical, dielectric, magnetic and optical properties arising from the strong interplay between their crystal structure, electronic configuration and transition metal–oxygen interactions. The perovskite manganites, with the general formula $Re_xAe_{1-x}MnO_3$, have received considerable attention owing to their multifunctional properties. In this formula, Re represents a trivalent rare-earth ion such as La or Nd, while Ae denotes a divalent alkaline-earth ion such as Sr or Ca. These materials have been extensively investigated for giant magnetoresistance (GMR), metal-insulator transitions and magnetic ordering involving charge, orbital and spin degrees of freedom. Colossal magnetoresistance has been reported in single crystals, thin films and ceramic manganites [1-3], stimulating extensive studies of their magnetic, electrical and magnetotransport properties. The metal-insulator transition and magnetic behaviour of doped manganites have been investigated in numerous studies [4-9].

Nanostructured magnetic materials have attracted interest for applications in magnetic sensors, data storage, magnetic fluids, refrigeration, catalysis and drug delivery. Size reduction to the nanoscale can modify the magnetoresistive response and magnetic characteristics of manganites, with effects such as enhanced GMR, superparamagnetic behaviour, reduced coercivity, lower Curie temperature (T_C) and decreased saturation magnetization. These size-dependent effects have motivated the development of nanostructured manganites. Dey & Nath [10] synthesized $La_{0.7}Ca_{0.3}MnO_3$ nanoparticles with magnetoresistance (MR) of 23%, while $La_{0.67}Sr_{0.33}MnO_3$ prepared by the same group exhibited an MR of nearly 20% [11]. To enhance the MR response, A-site substitution in $LaSrMnO_3$ with Sm, a rare-earth element with distinctive magnetic characteristics, was investigated, resulting in a substantial increase in MR [12-14].

The development of inorganic–organic hybrid nanocomposites has attracted considerable attention owing to their diverse application potential. Among conducting polymers, polypyrrole (PPy), polythiophene and polyaniline (PANI) have been extensively investigated [15-17]. In the present study, PPy was selected owing to its facile synthesis, good thermal stability, electrical conductivity and tunable optical, electrical, magnetic and chemical properties. PPy has further demonstrated considerable potential in surface modification strategies [18,19]. In our previous study on a PANI-$La_{0.67}Sr_{0.33}MnO_3$ nanocomposite, a substantial enhancement in magnetoresistance (MR), reaching 73%, was observed [20]. Motivated by this result, we also synthesized PPy-coated $La_{0.9-x}Sm_xSr_{0.1}MnO_3$ nanocomposites and compared their MR behaviour with that of the corresponding uncoated $La_{0.9-x}Sm_xSr_{0.1}MnO_3$ materials. The primary objective was to enhance the MR response, which is an important parameter for high-performance giant magnetoresistance (GMR) sensing devices. Remarkably, PPy coated $La_{0.9-x}Sm_xSr_{0.1}MnO_3$ nanocomposites exhibit an oscillatory magnetoresistance (MR) response, which, to the best of our knowledge, has not been reported for this system. This unusual magnetotransport behaviour provides a basis for exploring PPy-manganite nanocomposites as functional materials for spintronic and magnetic-sensing applications. Chang *et al*. [21] theoretically predicted orbital magneto-resistance (OMR) in magnetic semiconductors using different theoretical models, while Mamani *et al*. [22] reported non-linear transport behaviour and OMR in double quantum wells under magnetic fields below 1 T. The present results suggest that PPy-coated manganite nanocomposites may serve as promising candidates for advanced magnetotransport and spintronic applications.

EXPERIMENTAL

The chemicals *viz*. manganese acetate [$Mn(CH_3COO)_2$], samarium oxide (Sm_2O_3), lanthanum oxide (La_2O_3), strontium nitrate [$Sr(NO_3)_2$] were used. Cetyltrimethylammonium bromide (CTAB), triethanolamine (TEA), ammonium peroxodisulfate (APS), pyrrole, ethanol, acetone was procured from commercial sources. They were used as received or purified as necessary for the experiments.

Synthesis: Polypyrrole–$La_{0.9-x}Sm_xSr_{0.1}MnO_3$ nanocomposites (PM) were synthesized *via* a two-step process. In the first step, $La_{0.9-x}Sm_xSr_{0.1}MnO_3$ (M) nanoparticles were prepared using a pyrophoric reaction process [10]. An aqueous solution containing stoichiometric amounts of Sm_2O_3, La_2O_3, $Mn(CH_3COO)_2$ and $Sr(NO_3)_2$ was prepared. TEA was mixed in a molar ratio of TEA to metal ions equal to 4:1:1 (TEA: Mn: La, Sm, Sr). The resulting mixture was stirred continuously and heated on a hot plate until a viscous black, fluffy precursor was formed. This carbonaceous mass was then calcined at 1023 K to obtain nanocrystalline manganite powders. Five samples with varying samarium content (x = 0.1, 0.2, 0.3, 0.4 and 0.5) were prepared and labeled as M1, M2, M3, M4 and M5, respectively.

In second step, the synthesis of polypyrrole-manganite composite was performed by one pot oxidation of pyrrole in presence of manganite. M1 manganite powder was dispersed in an aqueous solution of CTAB by ultrasonication for a couple of hours. Pyrrole was poured into the dispersion of M1 and aqueous APS solution-an oxidant gradually added with continuous stirring. A meanwhile, whole stirred solution turned to the black indicating polymerization of pyrrole and the stirring continued for 10 h for the completion of the polymerization. Resulting solid nanocomposite was filtered and washed several times with solvents like water, alcohol and acetone. A similar procedure was adopted for synthesis of other manganites (M2, M3, M4 and M5) and their composite with PPy. The PPy-manganite nanocomposite was designated as PM1, PM2, PM3, PM4 and PM5, corresponding to samarium concentrations of x = 0.1, 0.2, 0.3, 0.4 and 0.5, respectively.

Characterization: Identification of phases of the powdered manganite and composite was done by PANalytical X'Pert Pro X-ray diffractometer having a filter of nickel, Cu$K\alpha$ radiation of λ = 1.5414 Å and scanning of the samples was done by from 2θ = 20-80º. Microstructural features were examined using transmission electron microscopy (TEM; JEOL JEM-2100) and field-emission scanning electron microscopy (FESEM; JEOL JSM-7600F). Molecular stretching and bending vibrations were investigated using Fourier-transform infrared (FTIR) spectroscopy (Bruker Tensor 27). Electrical transport measurements were performed on pelletized samples using a standard four-probe system equipped with a Keithley 2400 source meter, with resistance measured as a function of temperature and magnetic field up to 1 T. AC impedance measurements were carried out using a Keithley 4200A-SCS parameter analyzer/impedance measurement system. A constant current of 3 mA was applied and measurements were recorded over the temperature range of 2-300 K using a closed-cycle cryostat.

RESULTS AND DISCUSSION

XRD analysis: To establish the nanocrystalline nature and phase composition of the $La_{0.9-x}Sm_xSr_{0.1}MnO_3$ powders, structural charact-erization was carried out by X-ray diffraction (XRD) (Fig. 1). The as-prepared precursor powders were predominantly amorphous, whereas calcination at 1023 K resulted in the formation of single-phase nanocrystalline M powders. The diffraction patterns of both manganites (Fig. 1a-b) and their composites are consistent with an orthorhombic crystal struct-ure belonging to the *Pbnm* space group. The observed peak positions and indexing are consistent with the LCMO phase reported by Dey & Nath [10]. The diffraction peaks originate from the constructive interference of X-rays scattered by the crystallographic planes within the nanocrystalline samples. Average particle size (D) was estimated using the Scherrer's equation:

$$D = \frac{k\lambda}{\beta_{eff}\cos\theta} \quad (1)$$

where k, the shape factor is equal to 0.9, λ = 1.54 Å, θ = the Bragg angle corresponding to the most intense peak and β_{eff} = effective broadening of the peak, defined as: $\beta_{eff}^2 = \beta_m^2 - \beta_s^2$, with β_m and β_s representing the full width at half maximum (FWHM) of the sample and a standard silicon reference, respectively. The calculated grain sizes for the M1-M5 samples

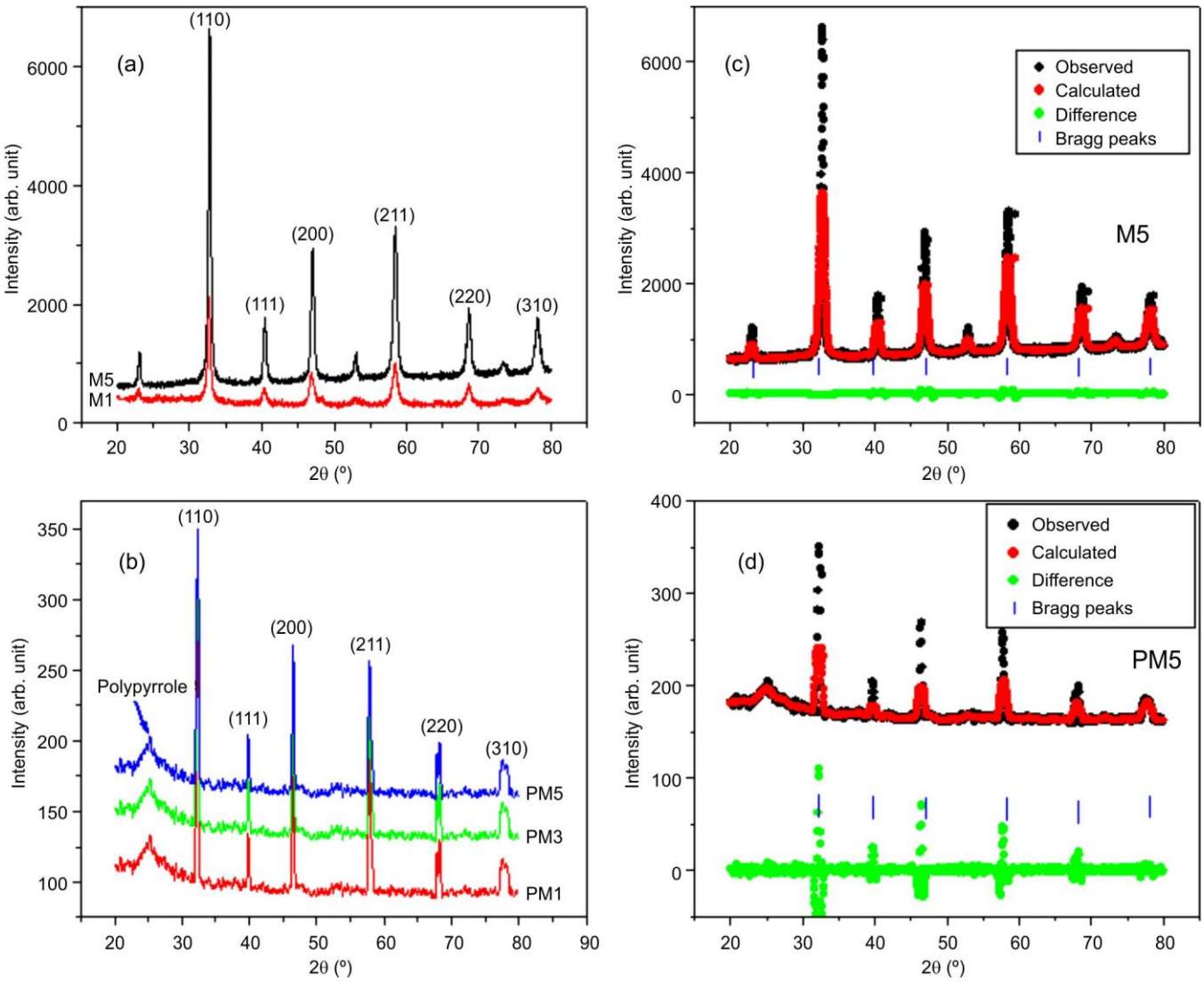

Fig. 1. (a) XRD pattern of manganate samples (M1 and M5) and (b) XRD pattern of nanocomposite (PM1-PM5), (c) Rietveld refinement of manganite (M5), (d) Rietveld refinement of nanocomposite (PM5)

ranged from 25 to 30 nm (± 0.003). Fig. 1b represents XRD patterns of both polypyrrole and nanocomposite. While polypyrrole is amorphous, the distinct peaks in the nanocomposite confirm the presence of crystalline manganite nanoparticles. The estimated grain sizes for the PM composites lie in the range of 30-35 nm (± 0.006), with the increase attributed to the polypyrrole coating surrounding the manganite cores.

To obtain reliable crystallographic information, Rietveld refinement of the XRD patterns was performed assuming an orthorhombic structure with *Pbnm* space group for manganite samples (M5). The refinement yielded lattice parameters of a = 5.412 ± 0.004 Å, b = 7.638 ± 0.006 Å and c = 5.368 ± 0.003 Å, with a unit-cell volume of 221.69 Å^3. The quality of the Rietveld refinement was assessed using the agreement indices R_p = 8.72%, R_{wp} = 11.43% and χ^2 = 2.05, which indicate a satisfactory agreement between the observed and calculated diffraction profiles. Rietveld refinement of the nanocomposite PM5 yielded lattice parameters of a = 5.42 ± 0.002 Å, b = 7.642 ± 0.004 Å and c = 5.371 ± 0.002 Å, corresponding to a unit-cell volume of 222.8 Å^3. The refinement parameters for PM5 were R_p = 8.2%, R_{wp} = 10.9% and χ^2 = 2.12, confirming a satisfactory fit between the experimental and calculated diffraction profiles.

Crystallite size and strain of both manganite and composite nanoparticles were also calculated using standard Williamson–Hall equation (eqn. 2). The equation is:

$$\beta\cos\theta = \frac{k\lambda}{D} + 4\varepsilon\sin\theta \qquad (2)$$

From this equation, an average crystallite size and microstrain of manganite M5 and PM5 were 33.5 ± 2.6 nm, 43 ± 2.1 nm, 1.1×10^{-3} and 1.8×10^{-3}, respectively. The close agreement between these values confirms the reliability of the size estimation and demonstrates that strain-induced broadening is relatively small.

FESEM analysis: Fig. 2 displays the FESEM micrographs of M1 and PM1, revealing a granular surface morphology in both samples. The estimated grain sizes are 20-30 nm for M1 and 30-40 nm for PM1. The larger apparent grain size of PM1 can be attributed to the polypyrrole coating surround-

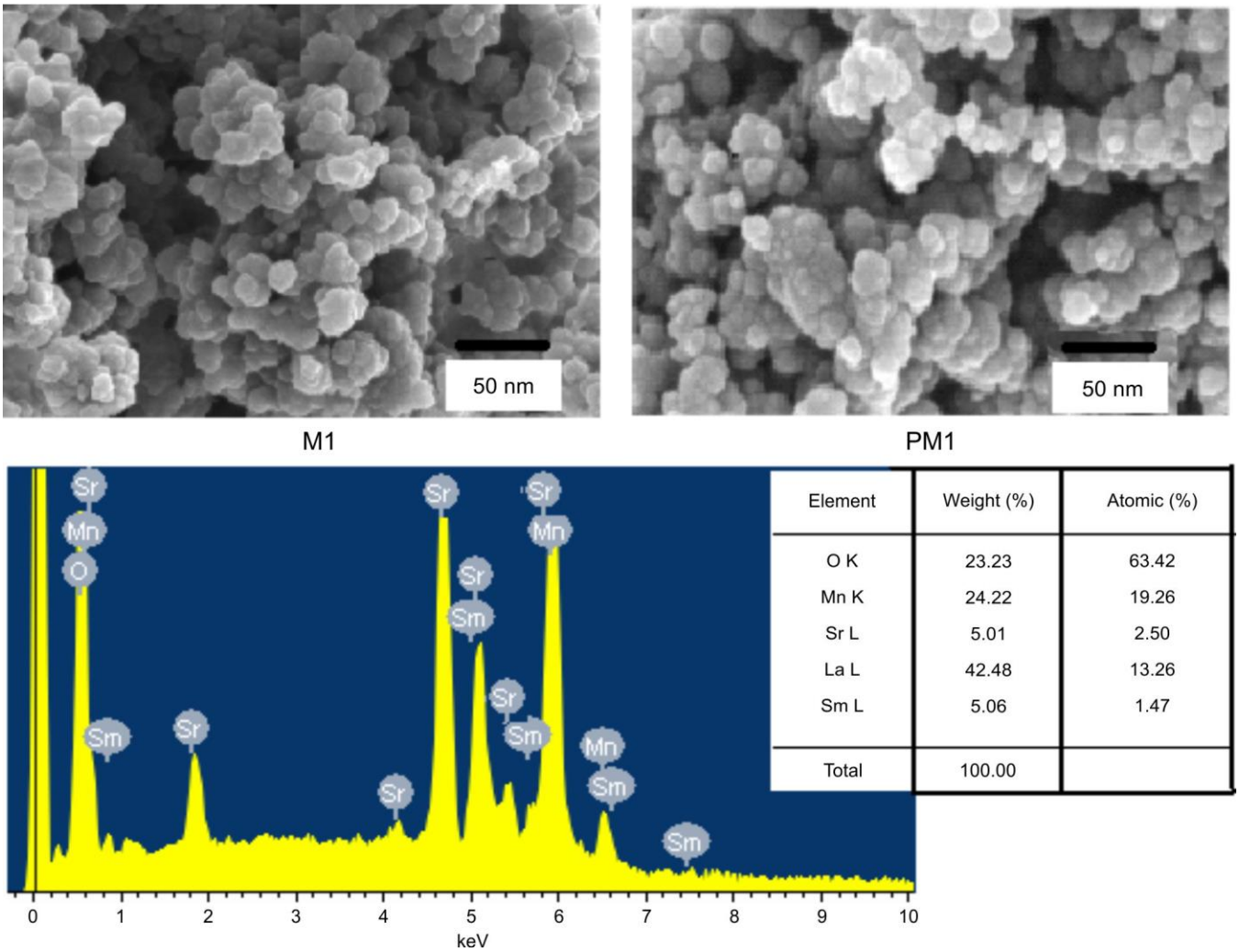

Element	Weight (%)	Atomic (%)
O K	23.23	63.42
Mn K	24.22	19.26
Sr L	5.01	2.50
La L	42.48	13.26
Sm L	5.06	1.47
Total	100.00	

Fig. 2. FESEM and EDS of manganite (M1) and nanocomposite (PM1)

ing the manganite nanoparticles. The corresponding EDS spectrum of M1 confirms the presence of La, Sm, Sr, Mn and O, consistent with the expected elemental composition of the manganite nanoparticles.

TEM analysis: The M1 micrograph (Fig. 3a) shows aggregated nanoparticles with predominantly spherical morphology and particle diameters of approximately 35 nm. The close packing of the nanoparticles may arise from interparticle magnetic and van der Waals interactions. The nearly spherical morphology and relatively uniform particle distribution support the formation of manganite nanoparticles.

The PM1-a (Fig. 3b) micrograph shows a more textured particle surface with increased interparticle spacing relative to M1, consistent with the formation of a polymer coating. In PM1-b (Fig. 3c), the particle boundaries exhibit reduced contrast, which can be associated with the lower electron density of the PPy layer surrounding the manganite core. The particle size is close to 45 nm. The schematic representation in Fig. 3 illustrates the proposed core-shell architecture, with the manganite core surrounded by a PPy shell.

Particle-size distribution histograms are presented in Fig. 3. M1 exhibits a near-Gaussian distribution over approximately 15-40 nm, with an average particle size of 27.0 ± 7.7 nm. PM1 exhibits a broader distribution extending from approximately 25-55 nm, with an average particle size of 41.8 ± 8.3 nm. The increase in particle size following PPy incorporation is consistent with the formation of a polymer coating around the manganite nanoparticles. The relatively symmetric size distributions indicate a comparatively uniform nanoparticle population.

The crystallite sizes estimated from XRD are slightly smaller than the particle sizes obtained from TEM. This difference is expected since XRD measures the size of coherently diffracting domains, whereas TEM provides the physical particle size, which may additionally include surface layers, agglomeration effects and the PPy shell surrounding the manganite core in the nanocomposites. Therefore, the observed discrepancy between XRD and TEM results is within the expected range for nanostructured materials.

FTIR analysis: The FTIR spectra of pure polypyrrole (P) and the manganite-polypyrrole nanocomposite (PM1) are shown in Fig. 4. The spectrum of pure polypyrrole exhibits characteristic bands at approximately 1580 and 1490 cm^{-1} assigned to C=C and C–N stretching vibrations associated with the quinoid and benzenoid units, respectively. The band at ~1290 cm^{-1} is attributed to C–N stretching, while the

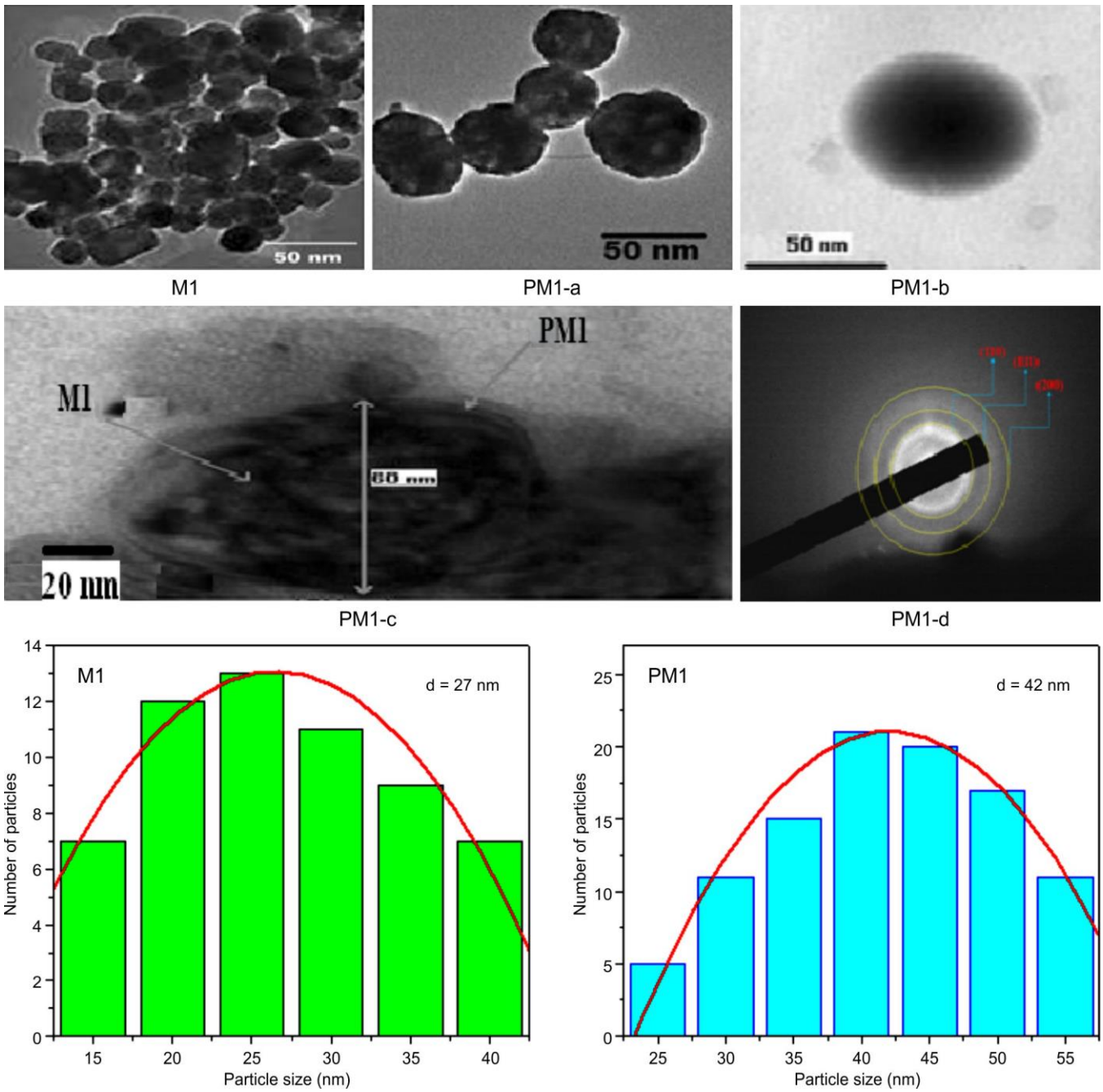

Fig. 3. TEM image of manganite nanoparticles (M1) and nanocomposite (PM1-a,b,c). SAED pattern of PM1-d. Particle size distribution of manganite (M1) and nanocomposite (PM1)

absorption at ~1140 cm^{-1} corresponds to in-plane deformation of the polypyrrole chain [23]. The bands near 820 and 502 cm^{-1} are assigned to C–H out-of-plane vibration and C–H bending vibration, respectively [23].

Following incorporation of manganite nanoparticles into the PPy matrix, the corresponding bands shift from 1580, 1490, 1290, 1140, 820 and 502 cm^{-1} to 1565, 1480, 1294, 1110, 790 and 490 cm^{-1}, respectively, accompanied by changes in band intensities. These spectral changes are consistent with interactions between surface sites of the manganite nanoparticles and functional groups along the PPy backbone, which may involve electrostatic interactions, coordination or hydrogen bonding. The FTIR spectrum of the manganite (M), presented in the inset of Fig. 4, provides additional evidence for the incorporation of the manganite phase within the composite [24-26].

DC electrical transport mechanism

In absence of magnetic field: Direct current resistivity of the samples was measured in presence and absence of magnetic field from low to room temperature. Resistivity of the manganite samples is more than that of the polypyrrole nanocomposite. With the increase in samarium content resistivity of manganites gradually decreases and in polypyrrole

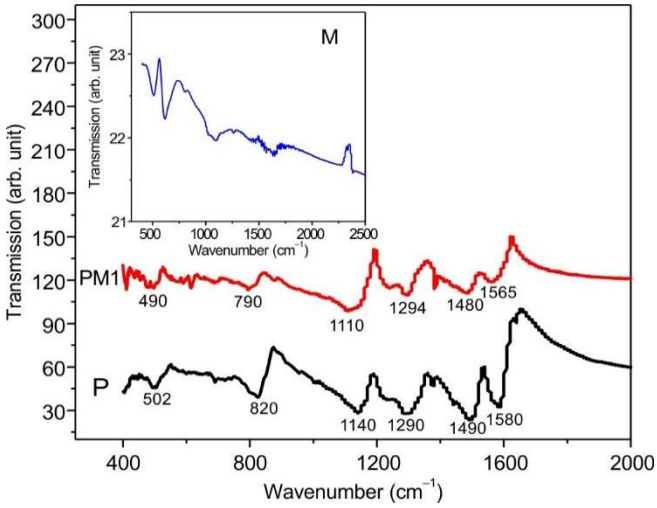

Fig. 4. FTIR spectrum of polypyrrole (P) and polypyrrole composite (PM1) [in the inset FTIR spectrum of manganite (M)]

nanocomposite, a similar trend of decreasing resistivity was found. Fig. 5a-b shows the temperature variation of the resistivity ρ(T) in absence of the magnetic field for manganite as well as polypyrrole nanocomposite. A semiconducting type of behaviour is obtained. This type of temperature dependence of resistivity can be well described by the Mott variable range hopping theory. According to this theory, resistivity can be expressed as:

$$\rho(T) = \rho_0 \exp\left(\frac{T_{Mott}}{T}\right)^{\gamma} \quad (3)$$

where ρ_0 is a constant, $T_{Mott} = \frac{24}{\pi k_B L_{loc}^3 N(E_F)}$ is the characteristics Mott temperature depending on the hopping barrier, electronic structure and energy distribution of the localized states, k_B is the Boltzmann constant, L_{loc} is the localization length and $N(E_F)$ is the density of states at the

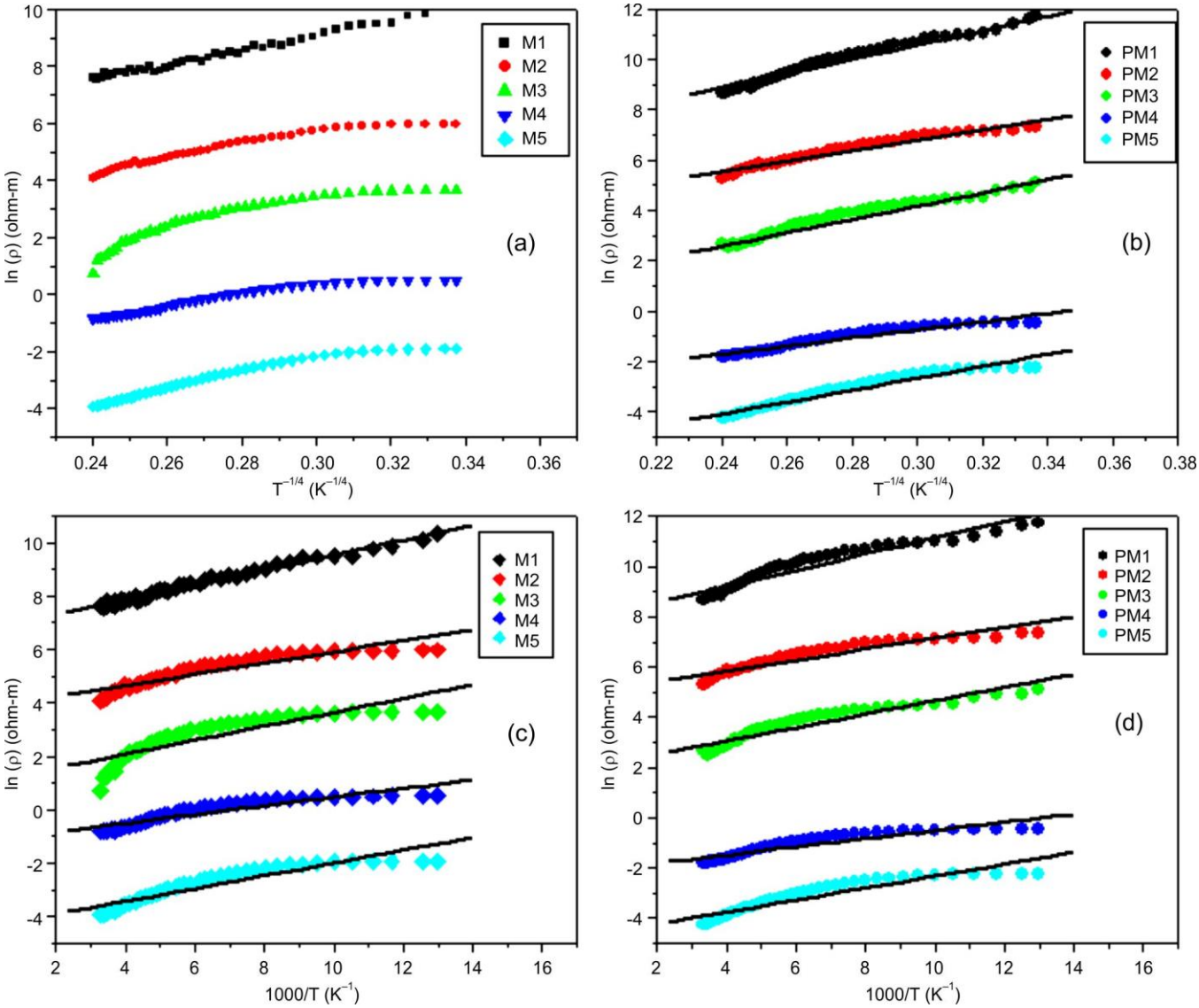

Fig. 5. (a) Temperature dependence of the dc conductivity of manganites and (b) temperature dependence of the dc conductivity of polypyrrole nanocomposite (c) ln ρ(T) *vs.* 1000/T plot for manganite for calculating activation energy. (d) ln ρ(T) *vs.* 1000/T plot for polypyrrole nanocomposite for calculating activation energy

Fermi level. γ is the VRH exponent from which the dimensionality of the conducting medium can be determined by the relation γ = 1/1+d. The possible γ values are 1/4, 1/3 and 1/2 for 3D, 2D and 1D system, respectively. A graph of lnρ(T) with $T^{-1/4}$ in Fig. 5a-b shows a linear variation indicating the 3D variable range hopping charge transport mechanism. T_{Mott} has been calculated from the slope of the curves of Fig. 5.

Although the temperature dependence of resistivity is satisfactorily described by the three-dimensional Mott variable range hopping model, an Arrhenius representation is additionally used to estimate effective activation energy associated with carrier hopping. This parameter serves only as a measure of the average transport barrier and facilitates comparison among different compositions; it should not be interpreted as evidence for an independent thermally activated band-conduction mechanism. Thus, the VRH model remains the primary description of charge transport in both manganite and polypyrrole nanocomposite. Thus, a graph (Fig. 5c-d) has been plotted between ln ρ(T) and 1000/T for both manganite and polypyrrole nanocomposite to calculate activation energy using the relation:

$$\rho(\%) = \rho_0 \exp\left(\frac{E_a}{k_B T}\right) \quad (4)$$

Activation energy varies from 22 to ~50 meV for manganite nanoparticles and 2 to 18.9 meV for the nanocomposite. Other extracted parameters for both manganite and PPy nanocomposite are given in Table-1, respectively. The extent of disorder can be measured in terms of resistivity ratio [ρ_r] and this ratio is higher in polypyrrole nanocomposite than manganites. So PPy coating on manganite nanoparticles may be the cause for disorder.

In presence of magnetic field: The magnetic field dependent resistivity of the samples was investigated under applied magnetic fields of up to 1 T. The observed magnetoresistance is negative and is evaluated using the standard relation $\left[\frac{\rho(B,T)-\rho(0,T)}{\rho(0,T)}\times 100\right]$. The introduction of samarium into LSMO leads to a systematic reduction in the magnetoresistance. The magnetoresistivity behaviour can be interpreted using a simple phenomenological framework that incorporates two concurrent hopping mechanisms: (i) the wave-function shrinkage model [27-31] and (ii) the forward-interference (orbital magnetoresistivity) model [32-34].

According to the wave-function shrinkage model, the application of a magnetic field suppresses the spatial overlap of localized electronic wave functions at neighboring sites, thereby increasing the electrical resistance with increasing field strength. In contrast, the forward-interference model accounts for constructive interference among multiple forward hopping paths between two sites separated by the optimum hopping distance, which leads to a decrease in resistivity and hence negative magnetoresistance. Thus, forward interference model will be the suitable for the explanation of negative magnetoresistance.

For small magnetic field, the magnetoresistivity ratio [29] can be expressed by eqn. 5:

$$\ln\left(\frac{\rho(B,T)}{\rho(0,T)}\right) = t_1 \frac{e^2 L_{loc}^4}{\hbar^2}\left(\frac{T_{Mott}}{T}\right)^{3/4} B^2 \quad (5)$$

where t_1 = 5/2016 and L_{loc} is the localization length. A plot of $\ln\left(\frac{\rho(B,T)}{\rho(0,T)}\right)$ *versus* B^2 was used to calculate L_{loc} for different samples and estimated values are ~ 65, 90,125, 150 and 180 Å, respectively for manganite samples.

Magnetic property: Variation of magnetization with magnetic field (8000 Gauss) at room temperature of the manganite nanoparticles and their nanocomposite with PPy have been studied (Fig. 6). Manganite nanoparticles (M5) exhibit a hysteresis loop and it indicates the presence of ferromagnetic ordering. Magnetization of M5 increases nearly linearly with the applied magnetic field upto 8000 Gauss and tends toward saturation at higher fields. A finite coercive field (H_c = 250-400 G) and remanent magnetization (M_r = 0.08-0.12 emu g^{-1}) are observed, consistent with the presence of ferromagnetic domains. The magnetization (Ms) reaches 1.40-1.45 emu g^{-1} at an applied field of 7000 G. The broader hysteresis loop of M5 points to stronger magnetic interactions than those in PM5.

The polypyrrole composite of manganite (PM5) also shows a hysteresis loop, but it is much narrower and slimmer than that of M5. The magnetization values are significantly smaller, with a maximum magnetization of only about 0.06 emu g^{-1} at 6000-7000 G. A small coercivity (H_c = 100-150 G) and remanence (M_r = 0.008) are observed, which indicate weak ferromagnetic behaviour with a tendency toward super para-

TABLE-1
PARAMETERS OF MANGANITES NANOPARTICLES AND POLYPYRROLE-MANGANITE NANOCOMPOSITE FROM THEIR DC ELECTRICAL TRANSPORT

Parameters	Manganites nanoparticles					Polypyrrole-manganite nanocomposites				
	M1	M2	M3	M4	M5	PM1	PM2	PM3	PM4	PM5
ρ (300 K) (Ω cm)	7.0×10^4	4.0×10^4	7.2×10^3	5.3×10^3	8.6×10^2	6.0×10^1	8.1×10^{-1}	5.2×10^{-1}	3.4×10^{-1}	1.2×10^{-2}
ρ_r (resistivity ratio)	1.0×10^{-3}	4.8×10^{-3}	3.8×10^{-2}	3.1×10^{-2}	4.0×10^{-2}	1.7×10^{-2}	1.8×10^{-2}	6.1×10^{-2}	2.6×10^{-1}	7.2×10^{-1}
γ	1/4	1/4	1/4	1/4	1/4	1/4	1/4	1/4	1/4	1/4
T_{Mott}	6.5×10^5	5.8×10^5	4.9×10^5	4.1×10^5	3.1×10^5	8.6×10^4	6.7×10^4	5.3×10^4	4.3×10^4	3.3×10^4
E_a (meV)	50.1	40.0	32.5	28.1	22.2	18.9	15.6	13.3	10.8	2.1

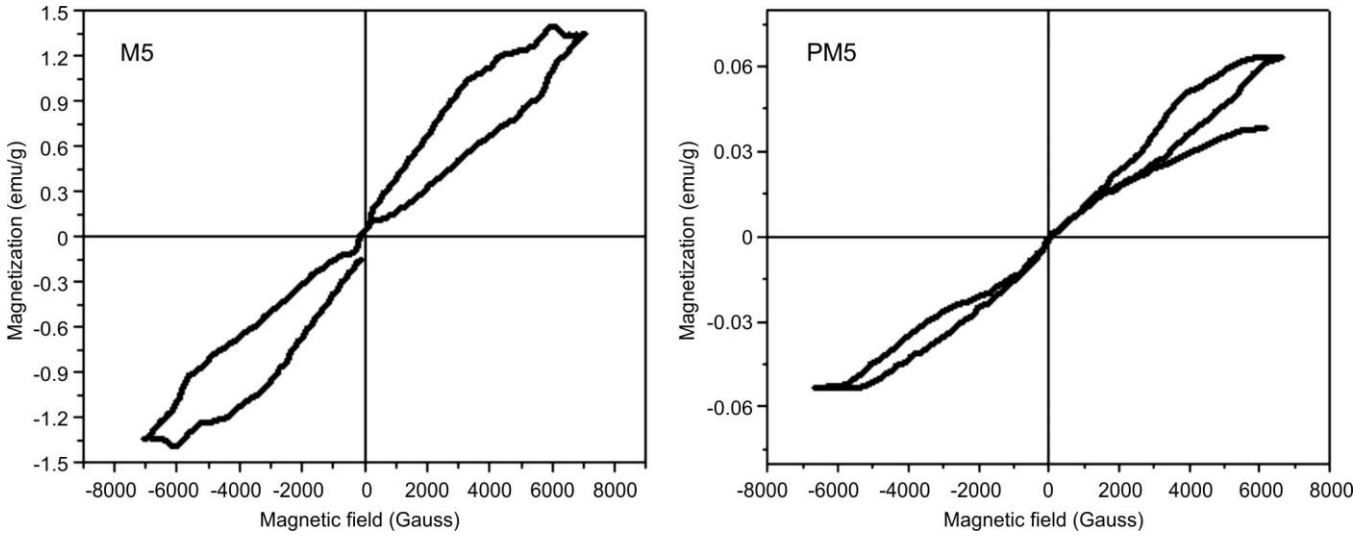

Fig. 6. Variation of magnetization with varying magnetic field at room temperature

magnetic or paramagnetic characteristics. The reduced loop area signifies weaker exchange interactions and lower magnetic anisotropy.

Effect of both magnetic field and temperature on resistance

For manganites nanoparticles: Fig. 7 shows the magnetic field dependence of MR for M1-M5 nanoparticles at 10, 50 and 250 K. The negative MR increases with increasing applied magnetic field. M5, corresponding to $La_{0.9-x}Sm_xSr_{0.1}MnO_3$ with x = 0.5, exhibits a maximum negative MR of approximately 75% at 50 K. The MR magnitude increases with Sm concentration and a similar composition-dependent trend is observed for the other samples. Such field-dependent MR is characteristic of polycrystalline manganites.

The field dependence of MR for M4 at different fixed temperatures is shown in Fig. 7. The MR magnitude decreases with increasing temperature, with the same temperature dependence observed for the other manganite compositions. Reported MR values for $La_{0.7}Ca_{0.3}MnO_3$ and $La_{2/3-x}Eu_xCa_{1/3-y}Sr_yMnO_3$ were 18-20%, 23% and 44-52%, respectively [10, 11]. The manganite nanoparticles investigated in the present work exhibit substantially higher MR values. The negative MR can be associated with two principal processes: suppression of spin fluctuations and tunneling of conduction electrons across grain boundaries. A similar mechanism has been proposed for $La_{0.67}Ca_{0.33}MnO_3$ by Dey *et al*. [11]. The rapid MR change at low magnetic fields can be attributed to progressive magnetic-domain alignment through domain-wall motion across the grain boundaries.

To investigate the temperature dependence of MR in the manganite, the total MR was divided into spin-polarized tunneling (MR_{PST}) and suppression of spin fluctuations (MR_{INT}) contributions, following the model of Raychaudhuri *et al*. [35,36], which considers spin-polarized transport across grain boundaries and domain-wall motion under an applied magnetic field, consistent with the framework of Helman & Abeles [37] that accounts for continuous domain-wall slippage across grain-boundary pinning centres. MR may be represented using this model (eqn. 6):

$$MR = -A\int_0^H f(k)dk - JH - kH^3 \quad (6)$$

here, k denotes the pinning strength of the domain boundaries, defined as the minimum magnetic field required to overcome a specific pinning barrier, while the grain boundaries are assumed to possess a distribution of pinning strengths described by the distribution function f(k), expressed as:

$$f(k) = A\exp(-Bk^2) + Ck^2\exp(-Dk^2) \quad (7)$$

A, B, C, D, J, H and k are considered as fitting parameters and were determined through experimental data. MR_{SPT} can be calculated using:

$$MR_{SPT} = -\int_0^H f(k)dk \quad (8)$$

Eqn. 6 was fitted to the experimental MR *versus* H data following the method described by Raychaudhuri *et al*. [35, 36]. Differentiation of eqn. 6 with respect to the magnetic field, followed by substitution of eqn. 7, yields:

$$\frac{d(MR)}{dH} = A\exp(-BH^2) + CH^2\exp(-DH^2) - J - 3kH^2 \quad (9)$$

The experimental MR–H curves were differentiated and fitted using eqn. 8 to extract the best-fit parameters at different temperatures. These parameters were then used in eqn. 6 to reproduce the experimental MR–H data of the manganite nanoparticles. The calculated curves exhibit good agreement with the experimental data. The experimental MR, spin-polarized tunneling contribution $MR_{SPT}(H)$ calculated from eqn. 8 and intrinsic contribution $MR_{INT}(H)$ are listed in Table-2 for the different manganite samples at 50 K. $MR_{SPT}(H)$ decreases rapidly with increasing temperature, whereas $MR_{INT}(H)$ exhibits a more gradual decrease.

Fig. 8 presents the temperature dependence of $MR_{SPT}(H)$ and $MR_{INT}(H)$ for M1 and M2, with both contributions decreasing as the temperature increases. The same temperature dependence is observed for M3, M4 and M5. The enhanced $MR_{SPT}(H)$ contribution, associated with spin-polarized tunne-

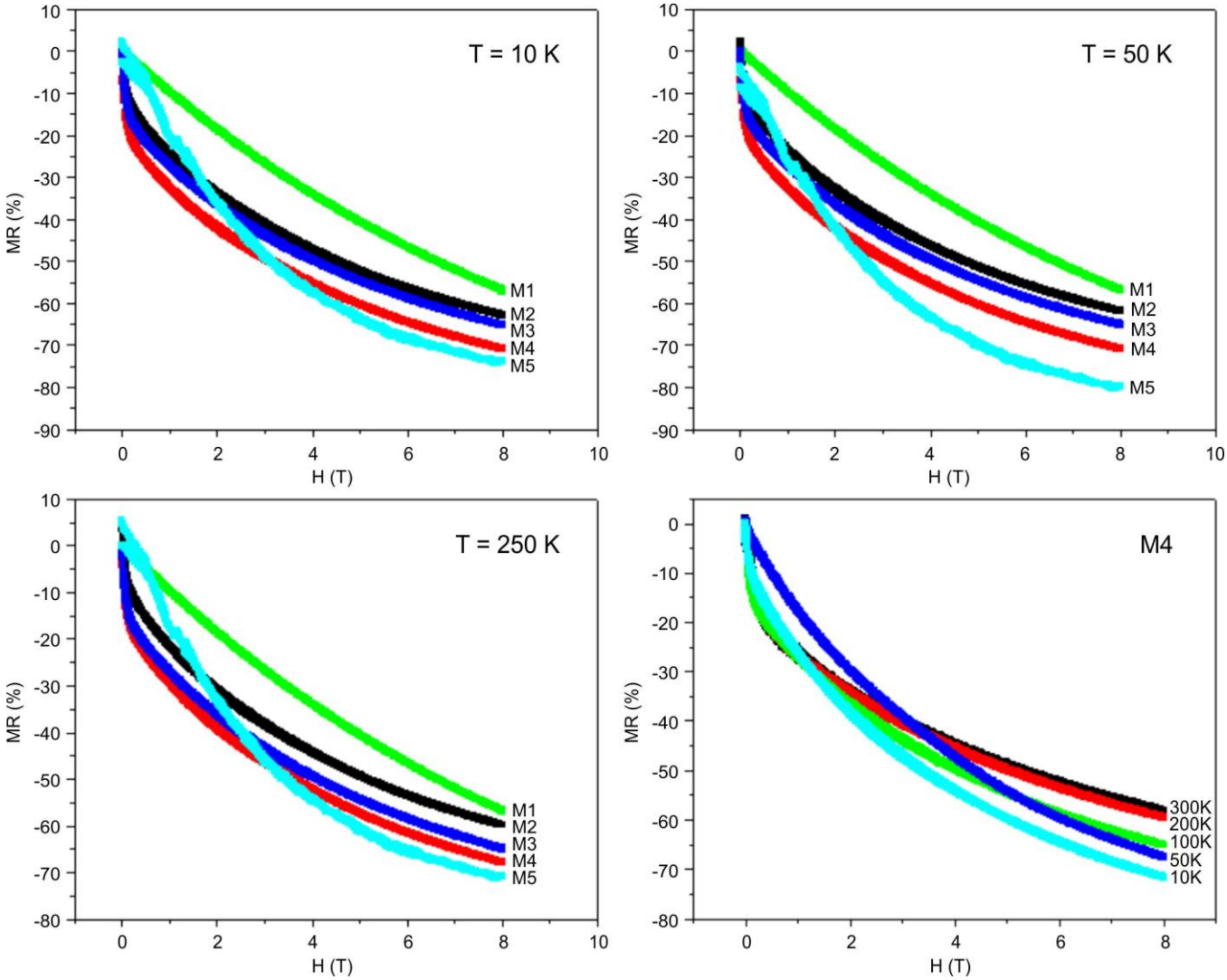

Fig. 7. Field variation of MR of different manganites at 10 K, 50 K and 250 K. Field Variation of MR at different constant temperature of M4

TABLE-2
EXPERIMENTAL MR, MR_{SPT}, MR_{INT} AT 50 K
FOR DIFFERENT MANGANITE SAMPLES

Sample No.	Experimental (MR%)	MR_{SPT} (%)	MR_{INT} (%)
M1	56.8	46.3	9.5
M2	61.7	52.4	8.1
M3	65.1	57.2	7.5
M4	71.6	64.4	6.9
M5	75.1	69.2	5.9

ling of conduction electrons between adjacent grains across grain boundaries, constitutes an important contribution to the high MR observed in the manganite nanoparticles.

For nanocomposite: At 10 K, PM1 exhibits an increasingly negative MR with increasing magnetic field (Fig. 9a) [38], a response that persists below 50 K and has been reported for other PPy-based nanocomposites. This low-temperature response can be associated with the presence of an insulating phase [38]. Fig. 9b presents the MR-field response of PM1 at different temperatures, which does not follow a well-defined conventional MR trend.

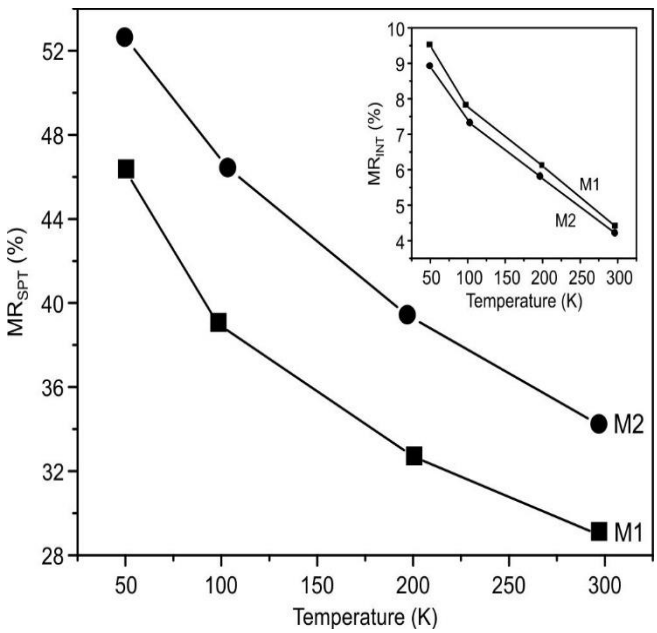

Fig. 8. Variation of MR_{SPT} and MR_{INT} with temperature

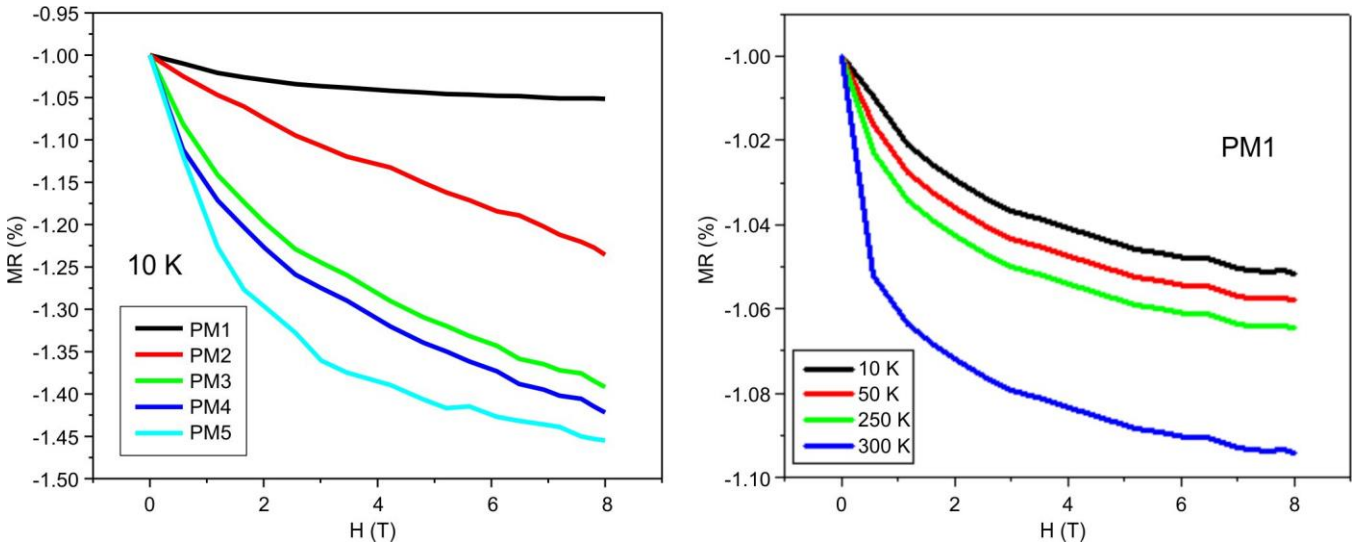

Fig. 9. Variation of MR with magnetic field of (a) PM1 to PM5 at 10 K and (b) PM1 at 10 K, 50 K, 250 K and 300 K

PM2 and PM3 exhibit pronounced oscillatory MR behaviour in the 50-250 K range (Fig. 10). The fluctuations are absent below 50 K and above 250 K for all investigated samples. Their intensity depends on the Sm concentration, with the strongest response observed for Sm concentrations of 0.2 and 0.3. The oscillatory MR response is consequently dependent on both temperature and composition. At 300 K, the fluctuation-like response disappears in PM1, PM2 and

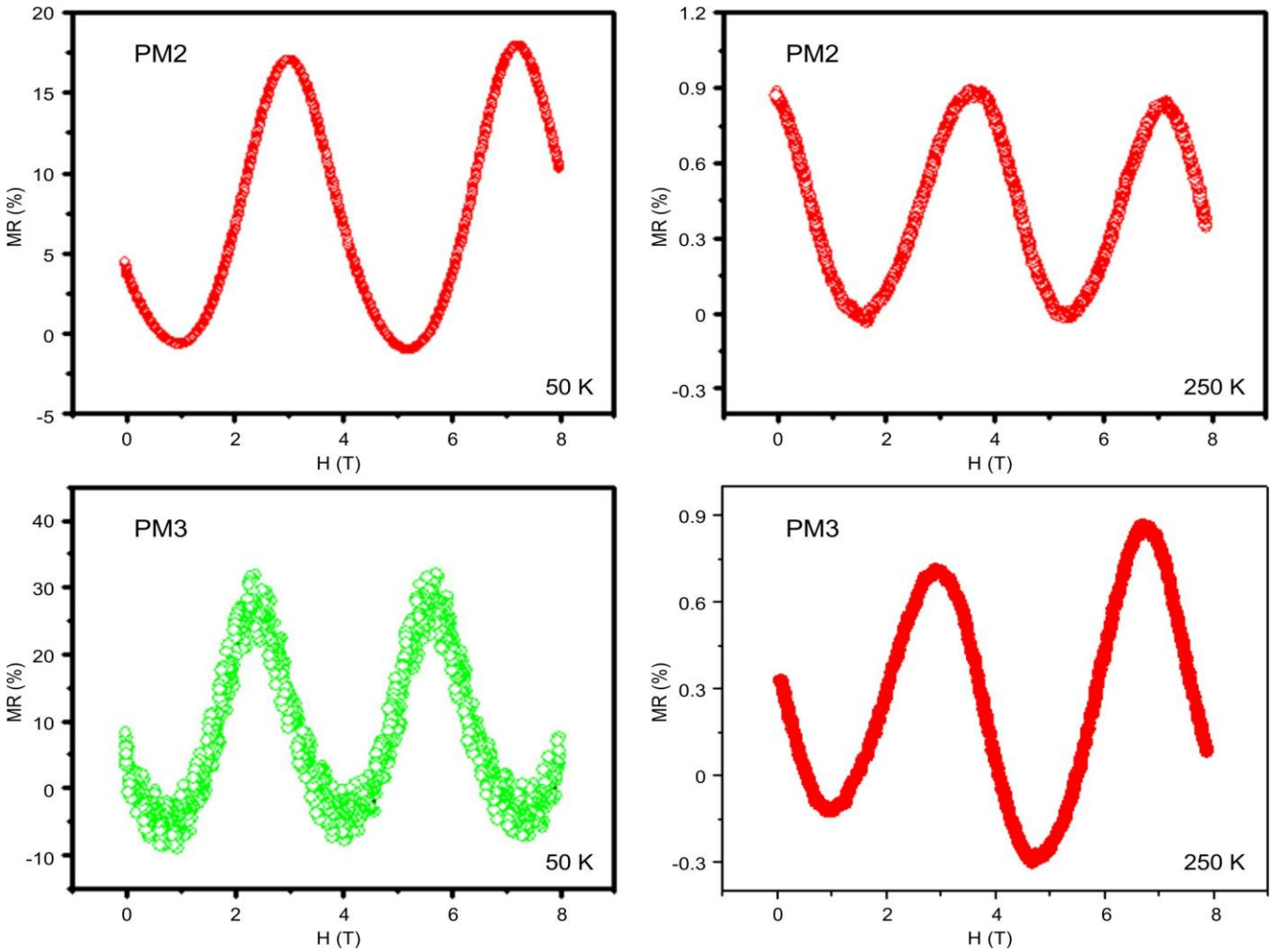

Fig. 10. Fluctuation-like field-dependent MR of PM2 and PM3 at 50 K and 250 K

PM3 (Fig. 11). PM4 and PM5 do not exhibit the anomalous oscillatory MR response; instead, they display a more complex composition-dependent MR variation over the investigated temperature range (Fig. 12), a feature not observed for PM1-PM3.

The incorporation of PPy introduces interfacial disorder and modifies the electronic and magnetic interactions within the manganite–polymer system. In a core-shell like architecture, the manganite/PPy interface can provide competing pathways for charge transport, with localization and delocalization of charge carriers influencing the field-dependent MR response. Interfacial exchange interactions and polymer-induced spin disorder can further modify spin alignment and spin-dependent transport. The relative contributions of these effects vary with temperature and Sm concentration, providing a plausible basis for the oscillatory MR response in PM2 and PM3 and the complex MR behaviour observed in PM4 and PM5. At elevated temperatures, enhanced thermal spin fluctuations within the PPy-coated system can further perturb spin-dependent transport and contribute to the complex field dependence of MR.

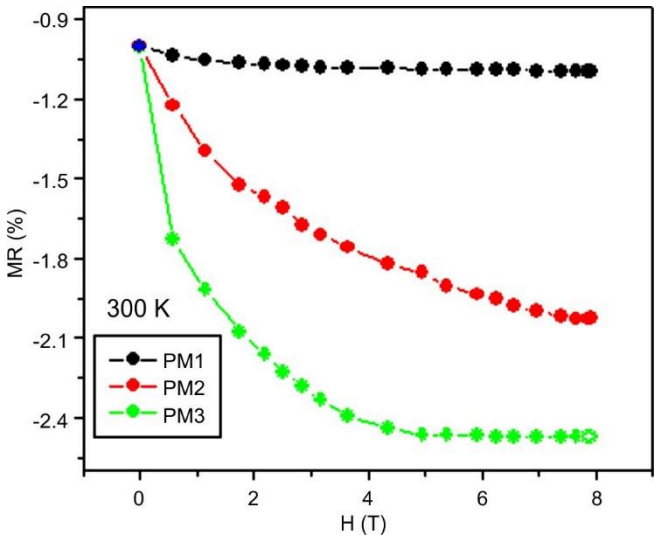

Fig. 11. Magnetoresistance at 300 K for PM1, PM2 and PM3

AC electrical transport mechanism: The AC conductivity of the manganite and nanocomposite samples was

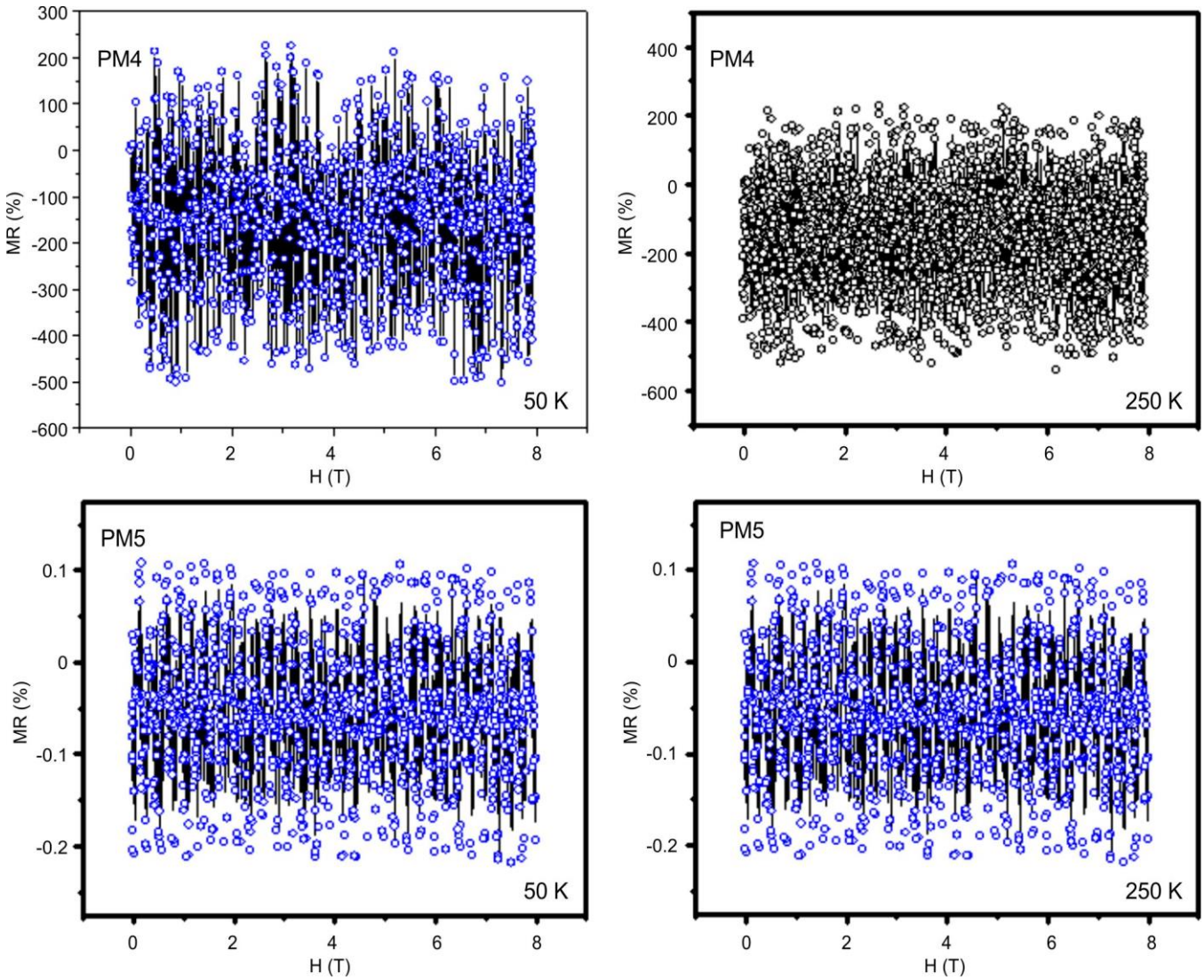

Fig. 12. Composition-dependent complex MR variation with varying magnetic field at 50 and 250 K for PM4 and PM5

measured over the temperature range up to 300 K and the frequency range of 20 Hz–1 MHz. The capacitance (C_p) and dissipation factor (D) were measured as functions of frequency. In disordered materials and amorphous semiconductors, the total electrical conductivity comprises a frequency-independent DC component (σ_{dc}) and a frequency-dependent AC contribution. At a fixed temperature, the frequency dependence of conductivity over a broad frequency range can be described by the universal dielectric response [39-41]:

$$\sigma'(f) = \sigma_{dc} + \sigma_{ac}(f) = \sigma_{dc} + \alpha f^{s} \qquad (10)$$

where α is a temperature-dependent constant, f is the measurement frequency and s is the frequency exponent with $s \leq 1$. At higher frequencies, the experimental conductivity follows the power-law dependence described by eqn. 10), while deviations at lower frequencies arise from the DC contribution. The AC conductivity, $\sigma_{ac}(f)$, was obtained by subtracting σ_{dc} from the total conductivity.

For M3, a linear dependence of $\ln[\sigma_{ac}(f)]$ *versus* $\ln(f)$ is observed at different temperatures (Fig. 13), with comparable behaviour obtained for the other manganite samples. The frequency exponent s, determined from the slope of these plots, decreases systematically with increasing temperature. Charge transport in disordered materials can occur through correlated barrier hopping (CBH) and quantum mechanical tunneling mechanisms [41,42]. The temperature dependence of s differs among the possible conduction mechanisms: s is nearly temperature independent for quantum mechanical tunneling, increases with temperature for small-polaron hopping, exhibits an initial decrease followed by an increase for large-polaron hopping and decreases monotonically with temperature in the CBH model. The observed decrease in s with increasing temperature is consistent with CBH as the dominant charge-transport mechanism in the manganite samples.

PM3 exhibits a similar linear dependence of $\ln[\sigma_{ac}(f)]$ on $\ln(f)$ at different temperatures (Fig. 13) and comparable behaviour is observed for the other nanocomposites. The systematic decrease in s with increasing temperature across the nanocomposite series is consistent with charge transport governed predominantly by the CBH mechanism

Conclusion

An investigation of DC and AC charge transport was carried out for manganite nanoparticles and their polypyrrole (PPy)-based nanocomposites. The pristine manganites exhibit conventional MR behaviour characteristic of polycrystalline materials, with MR increasing from 55% for M1 to 75% for M5 at 50 K, corresponding to enhanced MR with increasing Sm substitution. Analysis of the MR components shows that the spin-polarized tunneling contribution, $MR_{SPT}(H)$, is larger than the intrinsic contribution associated with suppression of spin fluctuations, $MR_{INT}(H)$, establishing spin-polarized electron tunneling across grain boundaries as the dominant source of the high MR. The temperature dependence of MR is consistent with this transport mechanism. The PPy-based nanocomposites exhibit pronounced oscillatory MR, with the response strongly dependent on temperature and Sm concentration. The fluctuation-like field-dependent MR is most pronounced for the lower-Sm compositions within the 50-250 K temperature range and can be associated with competing weak localization and charge-carrier delocalization. The observed behaviour is consistent with a core-shell like architecture involving intermediate exchange coupling between the magnetically ordered manganite core and the dis-ordered polymer-rich shell. The PPy layer plays an important role in modifying the interfacial magnetic and electronic inter-actions responsible for this response. The tunable magneto-transport characteristics of PPy-coated manganites provide scope for their investigation in spintronic and magnetic sensing applications, while the polymer–manganite platform offers flexibility for developing related nanocomposites with different polymer or ferrite components.

ACKNOWLEDGEMENTS

The authors gratefully acknowledge Nistarini College, Purulia, India, for its support during this work. The authors also acknow-

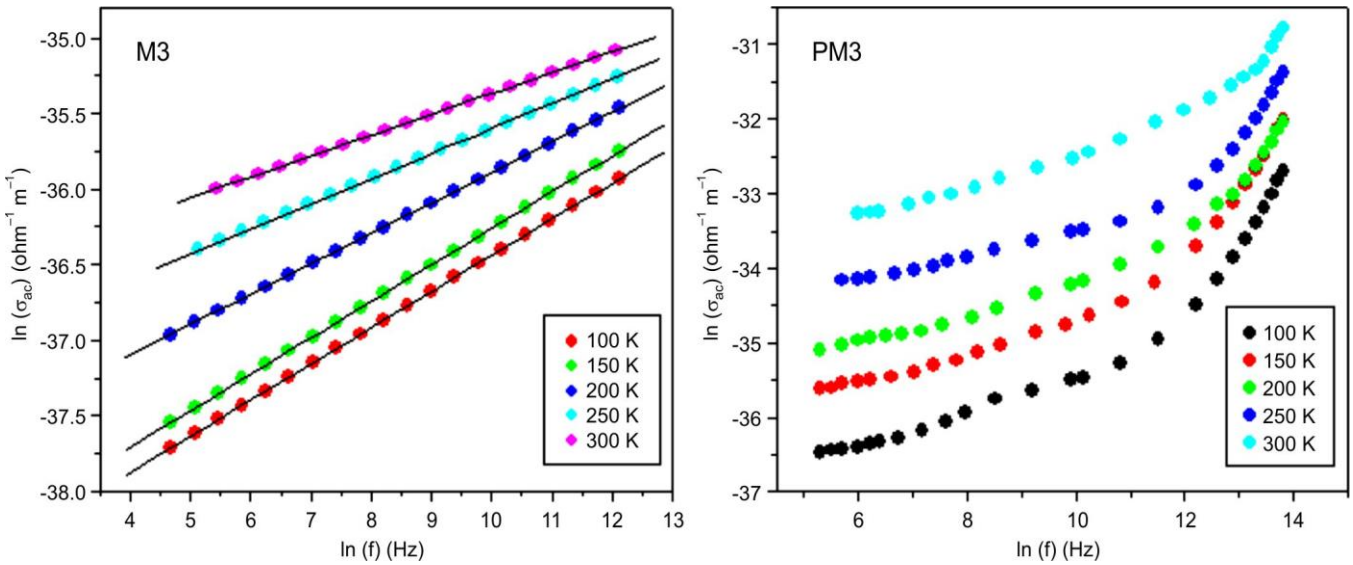

Fig. 13. Frequency dependent conductivity of manganite(M3) and polypyrrole nanocomposite (PM3)

ledge the Department of Physics, Vidyasagar University, Midnapore, India, for providing technical assistance.

CONFLICT OF INTEREST

The authors declare that there is no conflict of interests regarding the publication of this article.

DECLARATION OF AI-ASSISTED TECHNOLOGIES

During the preparation of this manuscript, the authors used an AI-assisted tool(s) to improve the language and no data, results or scientific conclusions were generated by AI. All analyses, interpretations and conclusions are the authors' own. The authors reviewed and edited the content and take full responsibility for the published work.

REFERENCES

1. E. Tafra, N. Novosel, Ž. Skoko, T. Ivek, M. Basletić, B. Mihaljević, Z. Jagličić, D. Rivas Góngora, A. Hamzić, V. Roddatis, F. Fischgrabe, V. Moshnyaga, S. Tomić, B. Korin-Hamzić and M. Čulo, *Phys. Rev. B*, **111**, 115107 (2025); https://doi.org/10.1103/PhysRevB.111.115107
2. A. Malisa and Z. Ivanov, *J. Magnet. Magnet. Mater*., **295**, 277 (2005); https://doi.org/10.1016/j.jmmm.2005.01.030
3. Y. Tokura, Colossal Magnetoresistive Oxides, Gordon and Breach, New York (2000).
4. N. Boora, R. Ahmad, S. Rahman, N.Q. Dung, M.B. Alshammari, A. Ahmad and B.-Il Lee, *Magnetochemistry*, **11**, 5 (2025); https://doi.org/10.3390/magnetochemistry11010005
5. K. Vladimir, M. Marchenko and Y. Melikhov, *Phys. Rev. B*, **82**, 064419 (2010); https://doi.org/10.1103/PhysRevB.82.064419
6. A.K. Pramanik and A. Banerjee, *Phys. Rev. B*, **81**, 024431 (2010); https://doi.org/10.1103/PhysRevB.81.024431
7. Z. Zhang, J. Li, W. Zhou, C. Yang, Q. Cao, D. Wang and Y. Du, *Ceram. Int*., **44**, 3760 (2018); https://doi.org/10.1016/j.ceramint.2017.11.159
8. J. Liu, Z. Du, S. Jiang, H. Shen, Z. Li, D. Xing, W. Ma and J. Sun, *J. Magnet. Magn. Mater*., **385**, 145 (2015); https://doi.org/10.1016/j.jmmm.2015.02.050
9. D.A. Bukreev, M.S. Derevyanko and A.V. Semirov, *Sensors*, **22**, 9512 (2022); https://doi.org/10.3390/s22239512
10. P. Dey and T.K. Nath, *Phys. Rev. B Condens. Matter Mater. Phys.*, **73**, 214425 (2006); https://doi.org/10.1103/PhysRevB.73.214425
11. P. Dey, T.K. Nath, U. Kumar and P.K. Mukhopadhyay, *J. Appl. Phys.*, **98**, 014306 (2005); https://doi.org/10.1063/1.1928307
12. M. Verhage, E.V. Minne, E.M. Kiens, L. Korol, R.J. Spiteri, G. Koster, R.J. Green, C. Baeumer and C.J. Flipse, *ACS Appl. Mater. Interfaces*, **16**, 21273 (2024); https://doi.org/10.1021/acsami.3c17639
13. A. Swain, K. Komatsu, M. Itoh, T. Taniyama and V. Gorige, *AIP Adv.*, **8**, 055808 (2018); https://doi.org/10.1063/1.5006597
14. U.K. Sinha, A. Sahoo and P. Padhan, *J. Alloys Compd.*, **952**, 170037 (2023); https://doi.org/10.1016/j.jallcom.2023.170037
15. K. Gupta, G. Chakraborty, S. Ghatak, P.C. Jana and A.K. Meikap, *J. Appl. Polym. Sci.*, **15**, 2911 (2010); https://doi.org/10.1002/app.31380
16. K. Gupta, G. Chakraborty, S. Ghatak, P.C. Jana, A.K. Meikap and R. Babu, *J. Appl. Phys.*, **108**, 073701 (2010); https://doi.org/10.1063/1.3489899
17. N. Asim, S. Radiman and M.A. Yarmo, *Mater. Lett.*, **62**, 1044 (2008); https://doi.org/10.1016/j.matlet.2007.07.051
18. G. Chakraborty, K. Gupta, A.K. Meikap, R Babu and W.J. Blau, *Solid State Commun.*, **152**, 13 (2012); https://doi.org/10.1016/j.ssc.2011.10.018
19. K. Gupta, P.C. Jana and A.K. Meikap, *Solid State Sci.*, **14**, 324 (2012); https://doi.org/10.1016/j.solidstatesciences.2011.12.003
20. K. Gupta, P.C. Jana, A.K. Meikap and T.K. Nath, *J. Appl. Phys.*, **107**, 073704 (2010); https://doi.org/10.1063/1.3360933
21. K. Chang, J.B. Xia and F.M. Peeters, *Phys. Rev. B Condens. Matter*, **65**, 115209 (2002); https://doi.org/10.1103/PhysRevB.65.115209.
22. N.C. Mamani, G.M. Gusev, O.E. Raichev, T.E. Lamas and A.K. Bakarov, *Phys. Rev. B Condens. Matter Mater. Phys.*, **80**, 075308 (2009); https://doi.org/10.1103/PhysRevB.80.075308
23. S. Bahraeian, K. Abron, F. Pourjafarian and R.A. Majid, *Adv. Mat. Res.*, **795**, 707 (2013); https://doi.org/10.4028/www.scientific.net/AMR.795.707
24. J.R. Xavier, J.R. Beryl, S.P. Vinodhini and G.B. Janaki, *J. Bio Tribocorros.*, **7**, 46 (2021); https://doi.org/10.1007/s40735-021-00479-7
25. B. Sevil and K. Zuhal, *Macromol. Symp.*, **295**, 59 (2010); https://doi.org/10.1002/masy.200900164
26. S. Gharbi, Y. Marouani, F. Issaoui, E. Dhahri, E.K. Hlil, R. Barille and B.F.O. Costa, *J. Mater. Sci.: Mater. Electron.*, **31**, 11983 (2020); https://doi.org/10.1007/s10854-020-03780-2
27. H. Liu, A. Pourret and P. Guyot-Sionnest, *ACS Nano*, **4**, 5211 (2010); https://doi.org/10.1021/nn101376u
28. B.I. Shklovskii, *Sov. Phys. JETP Lett.*, **36**, 51 (1982).
29. Y. Kajikawa, *Philosophical Mag.*, **106**, 277 (2026); https://doi.org/10.1080/14786435.2025.2564418
30. Y. Kajikawa, *Philosophical Mag.*, **103**, 1464 (2023); https://doi.org/10.1080/14786435.2023.2208884
31. R. Rosenbaum, H. Castro and W. Schoepe, *Physica B*, **294-295**, 486 (2001); https://doi.org/10.1016/S0921-4526(00)00706-7
32. V.L. Nguyen, B.Z. Spivak and B.I. Shklovskii, *JETP Lett.*, **41**, 42 (1985).
33. A.V. Shumilin and V.I. Kozub, *Phys. Rev. B*, **85**, 115203 (2012); https://doi.org/10.1103/PhysRevB.85.115203
34. H.A. Walling, E.G. Gwinn, K.D. Maranowski and A.C. Gossard, *Phys. Rev. B*, **71**, 045327 (2005); https://doi.org/10.1103/PhysRevB.71.045327
35. S. Ju, K.W. Yu and Z.Y. Li, *Phys. Rev. B*, **71**, 014416 (2005); https://doi.org/10.1103/PhysRevB.71.014416
36. P. Dey, T. K. Nath, *Appl. Phys. Lett*., **87**, 162501 (2005); https://doi.org/10.1063/1.2089179
37. J.S. Helman and B. Abeles, *Phys. Rev. Lett.*, **37**, 1429 (1976); https://doi.org/10.1103/PhysRevLett.37.1429
38. V. Dayal and V. Punith Kumar, *Solid State Commun.*, **158**, 70, (2013); https://doi.org/10.1016/j.ssc.2012.10.006
39. N.F. Mott and E.A. Davis, Electronic Processes in Non-Crystalline Materials, Oxford University Press, London, edn. 2 (1979).
40. M.N. Islam, S.K. Ram and S. Kumar, *Physica E*, **41**, 1025 (2009); https://doi.org/10.1016/j.physe.2008.08.047
41. S.R. Elliott, *Adv. Phys.*, **36**, 135 (1987); https://doi.org/10.1080/00018738700101971
42. V. Gvozdikov, *Phys. Rev. B*, 75, 115106 (2007); https://doi.org/10.1103/PhysRevB.75.115106